Electron-Cloud Simulations

G. Rumolo and F. Zimmermann, CERN, Geneva, Switzerland

Abstract

At CERN we presently perform two types of electron-cloud simulations. The first addresses the build-up of the electron cloud during the passage of a bunch train, the second the single-bunch instability which is induced by these electrons. We describe the essential ingredients and the underlying physics models for these simulations, and then present example results, such as the electron build up in the CERN SPS and the KEKB LER, the electron-cloud heat load in the LHC arcs, the electron densities in the damping rings of future linear colliders, and the short-range wake field for the CERN SPS.

1 INTRODUCTION

We model two different aspects of the electron-cloud phenomenon, for which we have written the programmes ECLOUD and HEADTAIL [1], respectively.

The first program ECLOUD simulates the build up of the electron cloud during the passage of a bunch train. It renders informations on the transverse electron distribution inside the vacuum chamber, the time evolution of both the total number of electrons and the electron density near the beam, the energy spectrum of electrons impinging on the wall, as well as their dose and azimuthal distribution, and the corresponding heat load, which is a concern for the LHC. The code allows the modelling of various magnetic (dipoles, quadrupoles, solenoids,...) and electric field patterns (clearing electrodes) as well as different vacuum chamber geometries. The simulated electron flux and energy spectrum are of interest for scrubbing-time estimates. The program can also be used to compute the bunch-to-bunch wake field due to the electron cloud, and indeed it was originally developed exactly for this purpose [2]. The bunch-to-bunch wake allows us to estimate the growth rate of the coupled bunch instability.

The second program HEADTAIL models the interaction of a single bunch with an electron cloud on successive turns. The cloud is assumed to be generated by the preceding bunches, and is taken to be initially uniform. Its density is inferred from parallel simulations with the ECLOUD code. The electrons give rise to a head-tail wake field, which amplifies any initial small deformation in the bunch shape, *e.g.*, due to the finite number of macroparticles. Without synchrotron oscillations, the resulting instability resembles the beam break up in a linac. If synchrotron motion is included, the instability becomes similar to the regular mode coupling instability. It induces a transverse centroid motion of the longitudinal bunch slices and also a substantial emittance growth. Both the bunch and the electrons are represented by macroparticles. A fresh uniform electron distribution is created prior to each bunch passage. For the purpose of the simulation, the electron cloud is concentrated at one (or more) locations around the ring. The interaction between the beam and electrons is calculated by computing the electric fields of either species on a two-dimensional grid, from which we then deduce the force exerted on the macroparticles of the opposite species. The interaction is calculated in steps, corresponding to the passage of the different bunch slices. Between turns, the beam macroparticles move from one slice to the next, as a consequence of their synchrotron motion. The program optionally includes the effect of nonzero chromaticity in both planes, the additional effect of a regular impedance, represented by a broadband resonator, and an additional betatron rotation which is proportional to the local beam density. Depending on whether this last rotation is applied around the center of the chamber, or around the center of each individual bunch slice, it models either a beam-beam interaction or a space-charge force.

The second program can be used to compute the single-bunch wake field, the single-bunch instability threshold, the instability growth rate above the threshold, the coherent tune shift and the incoherent tune spread. It also contains all informations necessary to extract the longitudinal wake field and the resulting potential-well distortion, as we illustrate in a companion paper [3]. In addition, synergetic effects between the electron cloud instability and beam-beam, space-charge, or impedance are studied easily. These studies show tantalising results; see Ref. [4], also in these Proceedings.

2 ELECTRON-CLOUD BUILD UP

2.1 Ingredients

The simulation programme for the electron-cloud build up has been described in Refs. [5, 6]. Figure 1 recalls the recipe and the main ingredients.

The primary photo-electrons (or ionization electrons) are represented by macroparticles. A typical number of 2000 macroelectrons is generated per bunch. Both the bunch and the interbunch gap are split into slices. During the passage of each bunch slice, new photoelectrons are created, in proportion the beam charge in that slice, and the existing macroelectrons are accelerated in the field of the beam and its image. The image forces are important for non-round vacuum chambers and if the beam is off-center. Whenever an electrons hits the wall, it is replaced by a secondary electron, and the charge of the electron is changed according to the secondary emission yield at the energy of the incident electron. In each inter-bunch gap the electrons are propagated in the external magnetic field. We always take into

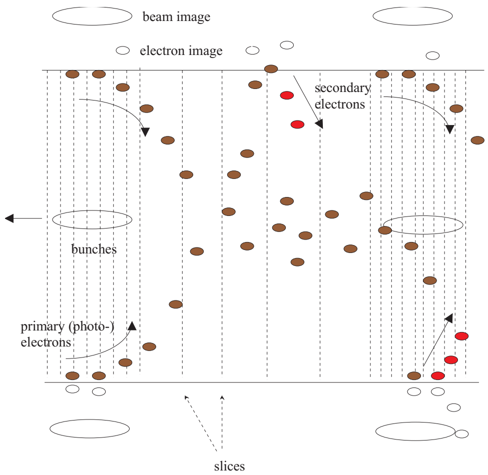

Figure 1: Schematic of simulation recipe.

account the electron space-charge field, which ultimately leads to a saturation of the electron build up, as well as the electron image charges.

Figure 2 displays the aperture considered in simulations of the LHC arc. It is a nearly round ellipse, which is flattened in the vertical direction. We do not have an exact analytical expression for the image charges in this geometry, and instead compute the image forces for the inscribed ellipse.

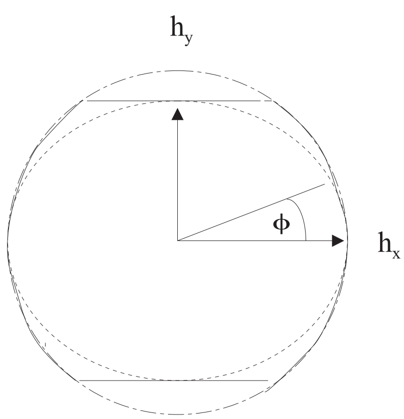

Figure 2: Transverse aperture in the LHC arcs. The solid line describes the actual cross section of the LHC beam screen. Sometimes we approximate it by the inscribed ellipse, *e.g.*, for accurate modelling of image charges.

For simulations of electron cloud in a dipole magnet, an important simulation parameter is the reflectivity R of the chamber wall. Most synchrotron radiation photons are emitted inside a narrow cone in the horizontal outward direction. In the presence of a vertical magnetic field, the photoelectrons emitted from this primary region of impact cannot approach the beam, since their motion is constrained to the vertical direction. The reflected photons can impinge on the top and bottom of the vacuum chamber, where photoelectrons can be directly accelerated towards the beam. If most of the circumference is occupied by dipole magnets, as in the LHC, only the fraction $(1 - R)$ of the primary photoelectrons will contribute to the electron-cloud build up. We typically assume that the reflected photons are distributed uniformly as a function of the azimuthal angle ϕ (see Fig. 2), measured from the center of the chamber, where $\phi = 0$ means horizontally outward and $\phi = \pi$ inward. However measurements done at BINP on a prototype LHC vacuum chamber suggest that the real distribution of the reflected photons is of the form $\cos^2[(\pi - \phi)/2]$ or even $\cos^3[(\pi - \phi)/2]$ [7].

The initial angular distribution of the newly generated primary photo-electrons is assumed to be uniform in the two spherical coordinates θ and ψ, defined with respect to the surface normal. The energy distribution of the emitted photoelectrons is modelled as a truncated Gaussian centered at 7 eV, with a standard deviation of 5 eV. This distribution does not approach zero for zero energies, which corresponds to a singularity in phase space, and may thus be in conflict with kinematic considerations, as has been pointed out by A. Chao [8]. However, the experimental data suffer from resolution limits near zero energy.

During a bunch passage electrons which are close to the center of chamber acquire a typical energy of up to a few hundred eV.

If the electrons are subjected to a strong magnetic field, they perform cyclotron oscillations. The number of cyclotron periods per bunch crossing can be large, *e.g.*, $eBc/(m_e c^2)\sigma_z/\pi \approx 120$ in an LHC dipole field at top energy ($B = 8.4$ Since, in addition, the Larmor radius is small, *e.g.*, 6 μm for a 200 eV electron in our LHC example, we often speed up the simulation by applying only a vertical acceleration during a bunch passage and ignoring the cyclotron motion in the orthogonal plane altogether. This simplification has first been proposed by S. Heifets [9].

In addition to the cyclotron motion, electrons can also oscillate in the beam potential, if they are close to the bunch. By contrast, electrons at sufficiently large amplitudes do not move during the bunch passage and simply receive a kick when the bunch passes by. The two situations have been called ‘autonomous region’ and ‘kick region’, respectively, by S. Berg [10], who has also computed the minimum number of simulation steps required for the autonomous region.

As a consequence of the oscillations in the beam potential, electrons starting near the bunch do not gain arbitrarily much energy during the bunch passage, but actually may be left with little energy after the bunch has gone. S. Berg [10] has computed the net energy gain of electrons as a function of their radial starting position, considering various bunch profiles. Following a similar line of thought, B. Richter [11] has pointed out that electrons can survive in the vicinity of the beam for a long time, if the bunch charge is high enough that electrons perform several oscillations inside the bunch, and the beam line density changes adiabatically.

Secondary electron energy distributions measured in the laboratory reveal reveal three components [12, 13]: (1) true secondaries at energies of a few eV, (2) elastically scattered electrons, whose energy is equal to the energy of the incident electron, and (3) re-diffused electrons, at intermediate energies.

The distinct contributions of true secondaries and reflected electrons can also be recognised in the measured curves of secondary emission yield versus primary electron energy. This is illustrated by a schematic in Fig. 3. The elastically reflected electrons are the more important the lower the primary energy. At very low energies, the elastic electrons completely dominate the secondary emission yield. A large probability of elastic reflection at low energies can significantly alter the simulation results. It also increases the minimum gap required to remove the electron cloud.

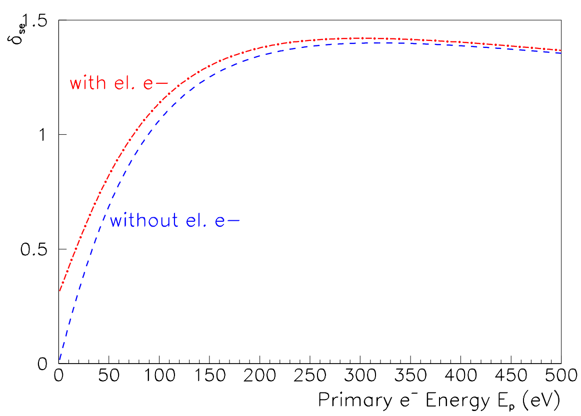

Figure 3: Secondary emission yield for perpendicular incidence vs. primary electron energy with and w/o elastically scattered electrons. The parametrization is based on recent measurements for a copper surface at CERN [13].

The term 'secondary emission yield' refers to the number of re-emitted electrons per incident electron. It is a function of the angle of incidence, the energy of the incident electron, and of the surface properties of the material. In particular the yield is not a constant in time, but may decrease due to electron bombardment or increase due to contamination. In the simulation, we treat the secondary emission yield as a sum of two components

$$\delta_{\rm se} = \delta_{\rm tse} + \delta_{\rm el}, \tag{1}$$

representing true secondaries and elastically scattered electrons, respectively. We do not separately consider the re-diffused electrons, but we assume a value for the yield in Eq. (1), which is consistent with the total yield measured.

In the past, the emission yield for the true secondaries has been approximated by the so-called Seiler formula [14]

$$\delta_{\rm tse}(E_{\rm p},\theta) = \delta_{\rm max}\, 1.11\, x^{-0.35}\, \left(1 - e^{-2.3x^{1.35}}\right) \\ \exp\left(0.5\,(1-\cos\theta)\right)\ , \tag{2}$$

where θ denotes the angle with respect to the surface normal, and [15]

$$x = E_{\rm p}\,\left(1 + 0.7(1-\cos\theta)\right)/\epsilon_{\rm max}\ . \tag{3}$$

There are only two parameters in this expression, the maximum yield at perpendicular incidence, $\delta_{\rm max}$, and the primary energy at which the yield is maximum, $\epsilon_{\rm max}$.

The yield for the elastic part was parametrized as [15]

$$\delta_{\rm el}(E_{\rm p}) = \delta_{{\rm el},0} + \delta_{{\rm el},E}\exp\left(-\frac{E_{\rm p}^2}{2\sigma_{\rm el}^2}\right)\ . \tag{4}$$

Whenever an electron hits wall, we throw a coin, that is we pick a random number r between 0 and 1. If the random number $r < \delta_{\rm el}/\delta{\rm se}$, we select an elastic reflection, in the other case, we generate one or more true secondaries. The code generates more than one true secondary, in case the product of yield and incident charge is larger than the charge of the initial primary macroelectrons.

The recent measurements on copper surfaces [13] were fitted using an alternative expression for the 'true secondaries' due to M. Furman [15]:

$$\delta_{\rm tse}(E_{\rm p},\theta) = \delta_{\rm max}\,\frac{sx}{s-1+x}\exp\left(0.5\,(1-\cos\theta)\right) \tag{5}$$

where $s \approx 1.35$ (N. Hilleret [13]), θ again denotes the angle with respect to the surface normal, $x = E_{\rm p}\,(1+0.7(1-\cos\theta))/\epsilon_{\rm max}$ as before.

Newly introduced was also an alternative expression for the yield of the elastically scattered electrons, which is written as a product of a function f and the true secondary yield [13]

$$\delta_{\rm el}(E_{\rm p}) = f(E_{\rm p})\delta_{\rm se}(E_{\rm p},\theta) \tag{6}$$

where the function f is obtained from measurements. For copper it has been parametrized as [16, 13]

$$\begin{aligned} f &= \exp\left(A_0 + A_1\ln(E_{\rm p}+E_0)\right. \\ &\quad \left.+A_2(\ln(E_{\rm p}+E_0))^2 + A_3(\ln(E_{\rm p}+E_0))^3\right)\,. \end{aligned}$$

For $E_{\rm p} < 300$ eV, the optimum coefficients are $A_0 = 20.7$, $A_1 = -7.08$, $A_2 = 0.484$, $A_4 = 0$, $E_0 = 56.9$ eV, while for larger energies, up to 2 keV, a better fit is obtained with $A_0 = -5.1$, $A_1 = 5.6$, $A_2 = -1.62$, $A_3 = 1.1\times10^{-5}$, $E_0 = 29$ eV. These revised formulae have recently been implemented in our simulation programme.

The emission angles of the true secondaries are distributed according to $dN/d\theta \propto \cos\theta\sin\theta$, or $dN/d\Omega \propto \cos\theta$, where Ω is the solid angle and θ the emission angle with respect to the surface normal. The initial energy distribution of the true secondaries is usually taken to be a half-Gaussian (centered at 0) with rms spread 5 eV. The same argument as made earlier for the energy distribution of the photoelectrons applies also here. Any distribution which does not decrease towards zero for zero energies violates kinematic constraints and appears unphysical [8].

Figure 4 displays four different initial energy distributions of secondary electrons, which can be optionally selected in the code. They correspond to a Gaussian, an exponential, a Lorentzian, and a distribution of shape Ee^{-E/E_0} (E_0 is some reference energy). The last distribution was proposed by M. Furman and it is the only one of tehse four which fulfills the kinematic constraints. The Lorentzian appears to be in best agreement with the measurements [17].

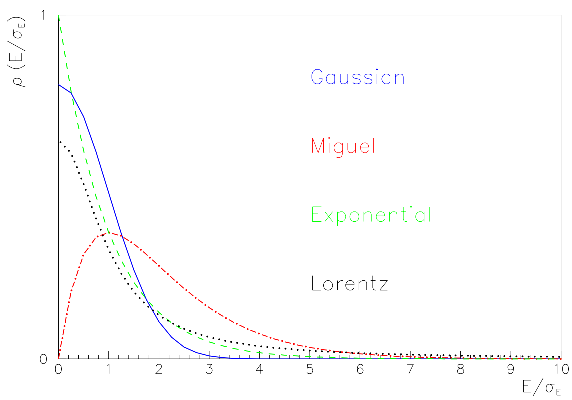

Figure 4: Four energy distributions of true secondaries which can be optionally selected.

We can try to derive an expression for the energy and angle distribution of the secondary electrons near energy zero. We assume that the inside the metal the relevant part of the energy distribution is a pure exponential $\propto \exp(-\bar{E}/E_0)$, characteristic of the scattering cascade, and that the angular distribution inside the metal is a $\cos\bar{\theta}\sin\bar{\theta}$ distribution, as found for higher energies. In order to overcome the surface potential the electron energy normal to the surface $\bar{p}_z^2/(2m_e)$ must exceed the work function $e\phi$ of the metal [17]. The tangential momentum component is unchanged when leaving the metal. The angles $\bar{\theta}$ inside and θ outside the metal are related via

$$\bar{\theta} = \frac{\theta}{\sqrt{1 + \frac{e\phi}{E}(1+\theta^2)}} \tag{7}$$

where E is the energy outside the metal. For energies much larger than the work function, the two angles are the same. Under the above assumptions, we find the following distribution function for the secondary electrons

$$\rho(E,\theta) \;\propto\; \exp(-E/E_0)\;\cos\bar{\theta}\sin\bar{\theta} \left| \frac{1+\frac{e\phi}{E}}{\left(1+\frac{e\phi}{E}(1+\theta^2)^{3/2}\right)} \right|, \tag{8}$$

where $\bar{\theta}(E,\theta)$ was given in Eq. (7), and the normalization constant has been dropped for simplicity. Equation (8) indicates a strong correlation between energies and angles for energies of the order of the work function. To which extent this correlation would be washed out by surface roughness is not clear. Equation (8) also suggests that for emission energies smaller than the work function, the density ρ increases approximately linearly with energy.

A recent empirical fit by N. Hilleret [18] of the measured energy spectra for the true secondaries emitted from copper to the formula [16]

$$\rho(E) = C \exp\left[-\frac{(\ln E/E_0)^2}{2\tau^2}\right] \tag{9}$$

yields a good representation of the measurements for $C \approx 0.2$, $E_0 \approx 1.8$ eV, and $\tau \approx 1$ [18]. Equation (9) shows the correct asymptotic behaviour at low energy, namely $\rho(E)$ approaches zero if E goes to zero.

Finally, we mention that the electrons also move longitudinally. The main contributions to this motion come from the initial longitudinal emission angle, the beam magnetic field, and, in a dipole magnet, from the $\vec{E}\times\vec{B}$ drift. Typical longitudinal velocities are of the order 10^5–10^6 m/s. The larger values apply to a field-free region, the smaller to a dipole field. Although this longitudinal motion is included in the code, it has no effect on the electron-cloud build up, since longitudinal distances travelled between the passages of subsequent bunches are much smaller than typical magnet lengths.

2.2 Results

Table 1 summarizes typical simulation parameters for various accelerators. Figure 5 shows the simulated electron-cloud build up for the LHC beam in the SPS. Only if the elastically scattered electrons are included, does the simulation predict a significant electron build and saturation at the center of the batch, in agreement with observations [19].

The saturation of the electron-cloud build up occurs at a line density of about

$$\lambda_{e,\mathrm{sat}} \sim N_b/L_{\mathrm{sep}} \approx 1.3\times10^{10}\ \ \mathrm{m}^{-1}, \tag{10}$$

where L_{sep} denotes the bunch spacing. The corresponding volume density is

$$\rho_{\mathrm{sat}} \approx \frac{N_b}{\pi h_x h_y L_{\mathrm{sep}}} \approx 3\times10^{12}\ \ \mathrm{m}^{-3}, \tag{11}$$

and the expected coherent tune shift due the cloud is estimated as

$$\Delta Q_{x,y} = \frac{h_{y,x}\beta_{x,y} C r_p \rho_e}{\gamma(h_x+h_y)} \approx 0.01 - 0.04, \tag{12}$$

where h_x and h_y denote the chamber half apertures.

Figures 6–9 shows simulation results for the KEKB LER. The first figure illustrates that the saturation density

Table 1: Simulation parameters for various storage rings.

symbol	LHC (init.)	LHC (fin.)	SPS	PS	KEKB
E [GeV]	7000	7000	26	26	3.5
N_b	10^{11}	10^{11}	10^{11}	10^{11}	3.3×10^{10}
$\sigma_{x,y}$ [mm]	0.3	0.3	3.0, 2.3	2.4, 1.3	0.6–1.0, 0.06–0.1
σ_z [cm]	7.7	7.7	30	30	0.4
$\beta_{x,y}$ [m]	80	80	40	15	15
L_{sep} [m]	7.48	7.48	7.48	7.48	
$h_{x,y}$ [mm]	22, 18	22, 18	70, 22.5	70, 35	47
$\delta_{\max}$	1.9	1.1	1.9	1.9	1.8
$\epsilon_{\max}$ [eV]	240	170	300	300	300
R [%]	10	5	100	100	10–100%
$d\lambda_e/ds$ [10^{-6} m^{-1}]	1230	615	0.25	0.05	2000–50000

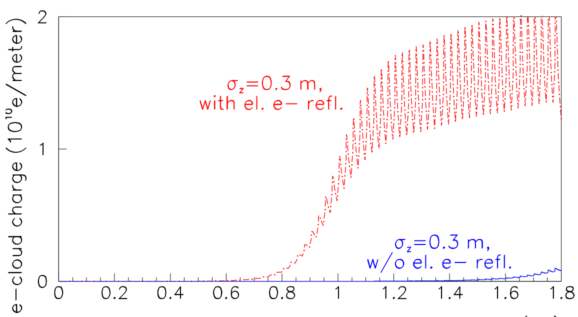

Figure 5: Simulated electron-cloud build up for an SPS dipole chamber, with and without elastic electron reflection [5].

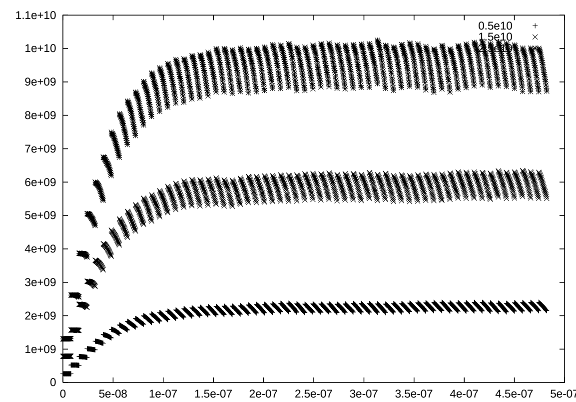

Figure 6: Simulated electron-cloud build up (total charge per meter) vs. time (s) in a field-free region of the KEKB LER for $N_b = 5 \times 10^9$, 1.5×10^{10}, 2.5×10^{10}), 4-bucket spacing, and a photoelectron yield of $Y = 0.05$/e$^+$/m [20].

increases in proportion to the bunch charge. Figures 7 and 8 compare the electron build up in a field-free region with that in a quadrupole and solenoid field. The solenoid suppresses the central cloud density by more than two orders of magnitude compared with the field-free case. The electron removal by a 1-kV clearing electrode is illustrated in Fig. 9.

Since the electron cloud presently limits the performance and blows up the positron beam sizes in the two B factories, it appears likely that it will also affect the positron beams in the damping rings of future linear colliders, which aim at generating beams of much smaller transverse emittances.

To investigate this possibility, we consider a set of typical parameters listed in Table 2, representing damping rings for CLIC [24] and NLC [23]. In the case of CLIC, we assume that both wiggler and arcs are equipped with an antechamber, which absorbs 95% of the photons. Only the remaining 5% contribute to the electron cloud generation via photoemission, with a supposed photoelectron yield of 5% per absorbed photon. We further assume that 10% of the photons escaping the antechamber are reflected towards

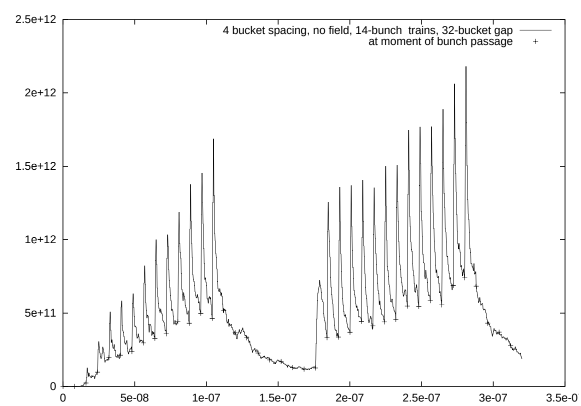

Figure 7: Electron density near beam per cubic meter for a field-free region as a function of time in seconds, during the passage of two bunch trains (4 bucket spacing) with a train-to-train gap of 32 buckets [20]. The simulation assumes $Y = 0.005$ and $R = 100\%$ [21].

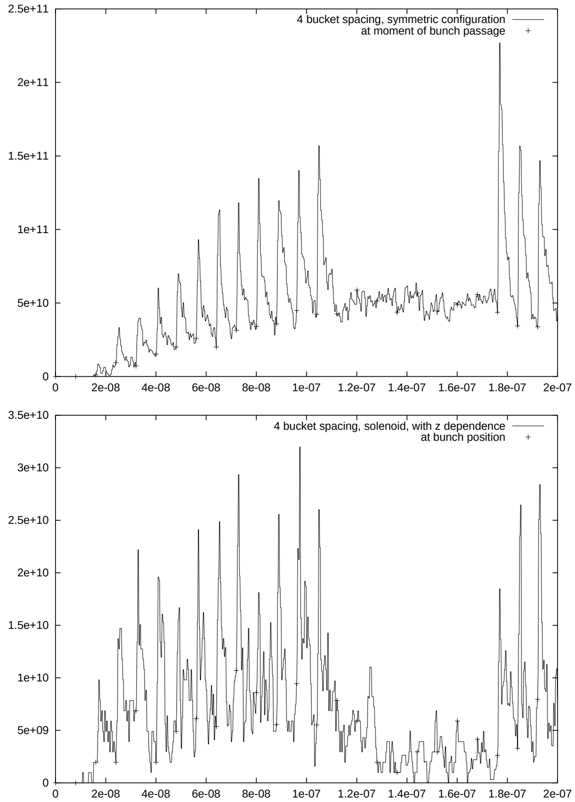

Figure 8: Simulated electron cloud density [m^{-3}] vs. time (s) in a periodic quadrupole configuration, with peak gradient of 0.5 T/m, minimum gradient 0.1 T/m and period 10 cm (top) and in a sinusoidal solenoid field with a peak field of ± 50G and 1-m longitudinal period (bottom), of the KEKB LER for $N_b = 3.3 \times 10^{10}$, 4-bucket spacing, $Y = 0.005$/e$^+$/m and $R = 100\%$ [21].

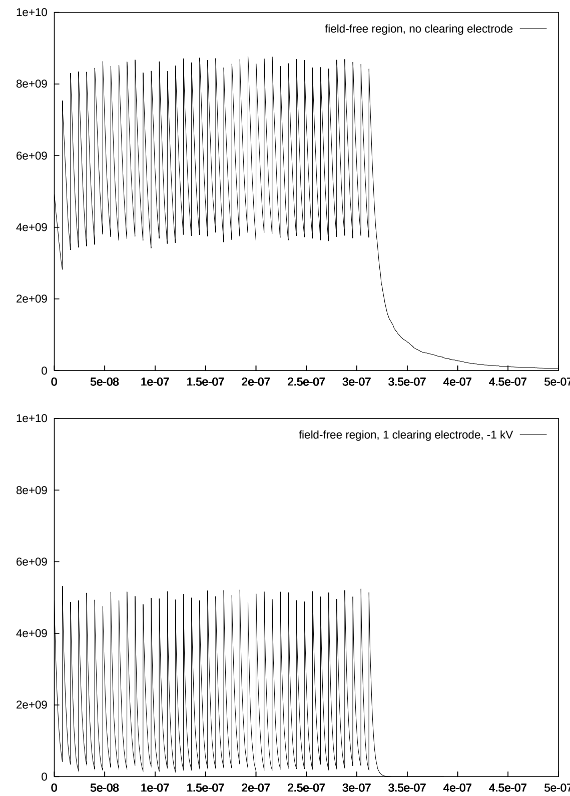

Figure 9: Electron line density in units of m^{-1} in a 1-m long magnetic field-free region vs. time in seconds, during and after the passage of a 40-bunch train without clearing electrodes (top), and with a single clearing electrode near the top of the chamber at approximately -1 kV (bottom) [22].

the top and bottom of the beam pipe, whereas the other 90% remain confined within a narrow outward cone. A photoelectron which impinges on the wall may be lost, reflected or produce true secondary electrons. The maximum secondary emission yield for perpendicular incidence will vary as a function of the electron dose already deposited. We consider values of $\delta_{\max}$ between 1.7 and 1.1.

In the CLIC damping rings, the dominant region of synchrotron radiation will be the long wiggler sections. Typical wiggler parameters are also listed in the table. In addition, there is of course synchrotron radiation in the arcs as well. We have simulated the electron-cloud build up for (1) a field-free region, (2) a bending field, (3) a periodic wiggler field, in all three cases considering a beam pipe illuminated by the wiggler radiation, and (4) for an arc dipole section, where the number of photoelectrons is reduced.

We have also performed a simulation for a field-free bellows section in the NLC damping ring. In this case we consider rather pessimistic parameters, provided by M. Pivi. In particular, no antechamber is considered, the photoelectron yield per absorbed photon is taken to be 20%, and the maximum secondary emission yield is assumed to be as high as $\delta_{\max} = 2.75$.

Results of the simulations for CLIC are displayed in Figs. 10–11. Figure 10 shows the evolution of the line density along the bunch train. It saturates at values of order 10^{10} m^{-1}. The electron density in the wiggler is higher than that in the arc (the latter not shown), due to the larger number of primary photoelectrons. The difference between the periodic wiggler magnet and a uniform dipole field is small, assuming the same primary electron production rate. Figure 11 displays the central cloud density near the beam. This central density assumes values up to a few 10^{14} m^{-3}, which is hundred times higher than the simulated and measured densities for the SPS or the two B factories, indicating that the electron cloud might pose a severe problem for the damping ring.

Figure 12 shows the simulated evolution of the electron line density for the NLC damping ring. It saturates around 3×10^{10} m^{-1} and thus is of similar size as for CLIC. The figure also demonstrates that the electron density decreases by about a factor of 3, if elastically reflected electrons are not taken into account in the simulation.

Table 2: Simulation parameters for future linear-collider damping rings [24, 23].

variable	symbol	CLIC	NLC
beam energy	E	3.5 GeV	1.98 GeV
bunch population	N_b	4.2×10^9	1.5×10^{10}
number of bunches per train	n_b	154	100
rms bunch length	σ_z	5 mm	3.6 mm
rms transv. beam size	$\sigma_{x,y}$	18, 1.5 μm	41.5, 9.0 μm
average beta function	β_y	5 m	5 m
norm. hor. emittance	$\gamma\epsilon_x$	4.5×10^{-7} m	3×10^{-6} m
norm. vert. emittance	$\gamma\epsilon_y$	3×10^{-9} m	3×10^{-8} m
bunch spacing	$L_{\rm sep}$	0.2 m	0.84 m
wiggler pole length	$l_{\rm pole}$	5 cm	
wiggler period	$l_{\rm w}$	20 cm	
peak wiggler field	B_w	1 T	
wiggler deflection	θ_w	4.1 mrad	
arc field	B_a	0.015 T	
chamber radius	$h_{x,y}$	5 mm	16 mm
primary electron rate in wiggler	$d\lambda_e/ds$	0.075 /e$^+$/m	
primary electron rate in arc	$d\lambda_e/ds$	0.0025 /e$^+$/m	6.1 /e$^+$/m
photon reflectivity	R	10%	10%–100%
maximum secondary emission yield	$\delta_{\rm max}$	1.1–1.7	2.75
energy of maximum sec. em. yield	$\epsilon_{\rm max}$	300 eV	315
probability of elast. reflection for $E_{\rm p} \approx 0$	$\delta_{{\rm el},E}$	0.56	0
width of elastic reflection	$\sigma_{\rm el}$	52 eV	–

The simulated electron densities imply severe consequences on the beam stability. The threshold density for the single-bunch TMCI instability driven by the electron cloud can be estimated as [25]

$$\rho_{e,{\rm th}}^{\rm TMC} \approx \frac{2\gamma Q_s}{\pi T_0 r_e c \beta_y} \; . \tag{13}$$

Assuming $cT_0 \approx 6$ km, $\beta_y \approx 5$ m, $E = 3.5$ GeV, and $Q_s \approx 0.02$, we estimate for CLIC a threshold density of $\rho_{e,{\rm th}}^{\rm TMC} \approx 10^{12}$ m^{-3}, hundred times smaller than the electron density simulated.

The coherent tune shift due to the cloud is [26, 27]

$$\Delta Q_{x,y} \approx \frac{\beta_{x,y} C r_e \rho_e}{2\gamma} \tag{14}$$

which, with $C \approx 6$ km, $\beta_{x,y} \approx 5$ m, $E \approx 3.5$ GeV, and $\rho_e \approx 10^{14}$ m^{-3}, evaluates to $\Delta Q_{x,y} \approx 0.6$! The incoherent tune spread can be several times larger still [26, 27].

In view of these numbers, it is likely that the electron-cloud issues will affect the overall design parameter optimization of a future linear collider.

Fortunately, the multipacting process itself reduces the secondary emission yield in the course of time, a phenomenon referred to as 'surface scrubbing'. The electrons incident on the chamber wall condition the surface in such a way that the secondary emission yield decreases. Thus, the electron yield depends on the electron dose that has previously been deposited on the surface [13]. Only electrons with sufficiently high energy contribute to the scrubbing. The simulated effective electron bombardment rate for an LHC beam in the SPS is shown in Fig. 13. Together with laboratory measurements of the conditioning effect as a function of dose, simulations like this can be used to estimate cleaning times and to decide about commissioning scenarios.

The energy spectrum of the incident electrons determines the efficiency of the surface scrubbing. Figure 14 shows, for an SPS example, that the energy spectrum changes with the bunch length.

Figure 15 illustrates the variation of the energy spectrum with the vacuum-chamber radius, using simulations for the LHC interaction regions as an example [29].

Figures 16 shows that in the LHC the magnetic field of the beam noticeably affects the electron impact angles. In the code, the effect of the beam magnetic field was added to the deflections arising from the electric field (super-index 'e') so as to obtain the total momentum changes (super-index 'em'):

$$\Delta p_{e,x}^{(em)} = \Delta p_{e,x}^{(e)} \left(1 - \frac{v_{e,z}}{c}\right) \tag{15}$$

$$\Delta p_{e,y}^{(em)} = \Delta p_{e,y}^{(e)} \left(1 - \frac{v_{e,z}}{c}\right) \tag{16}$$

$$\Delta p_{e,z}^{(em)} = \frac{v_{e,x}}{c} \Delta p_{e,x}^{(e)} + \frac{v_{e,y}}{c} \Delta p_{e,y}^{(e)} . \tag{17}$$

In particular, the beam magnetic field introduces a longitudinal deflection which the electric field does not.

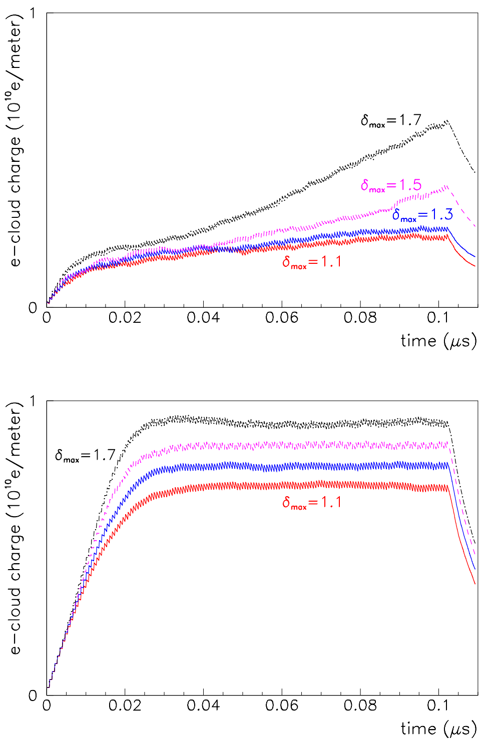

Figure 10: Electron line density in units of 10^{10} m^{-1} vs. time in μs, for the periodic wiggler in the CLIC damping ring (top) and the field-free region behind the wiggler (bottom) [24].

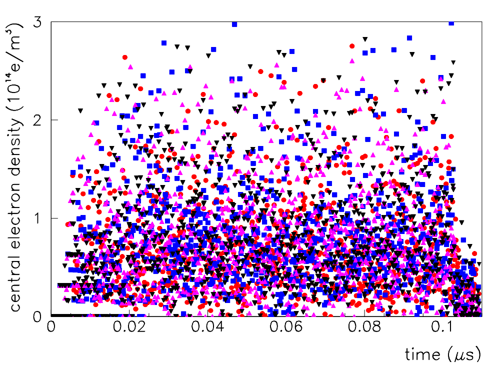

Figure 11: Evolution of central electron density in units of 10^{14} m^{-3} vs. time in μs, for a field-free region behind the CLIC wiggler. [24].

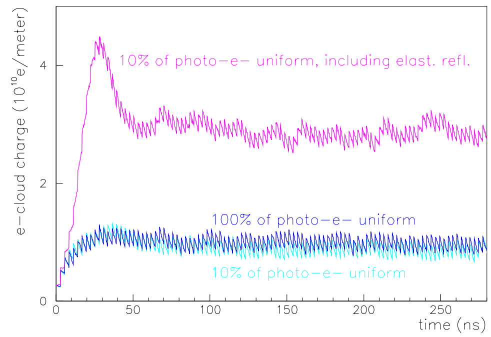

Figure 12: Electron line density in units of 10^{10} m^{-1} vs. time in μs, for a bellows section in the NLC damping ring.

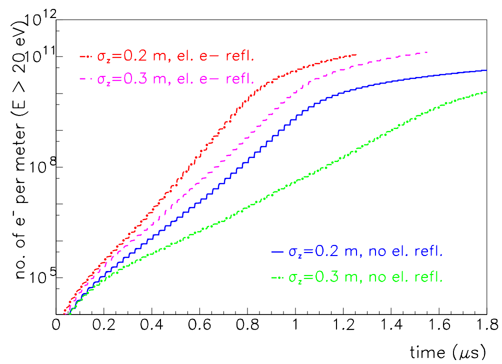

Figure 13: Simulated number of electrons per meter with energy $E > 20$ eV hitting the chamber wall during the passage of the 81-bunch LHC batch through an SPS dipole chamber, for $N_b = 4.3 \times 10^{10}$ (May 2000 parameters).

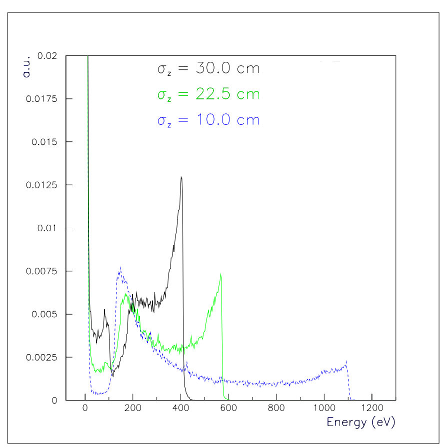

Figure 14: Simulated electron-cloud energy spectrum for different bunch lengths in a field-free region of the SPS [28].

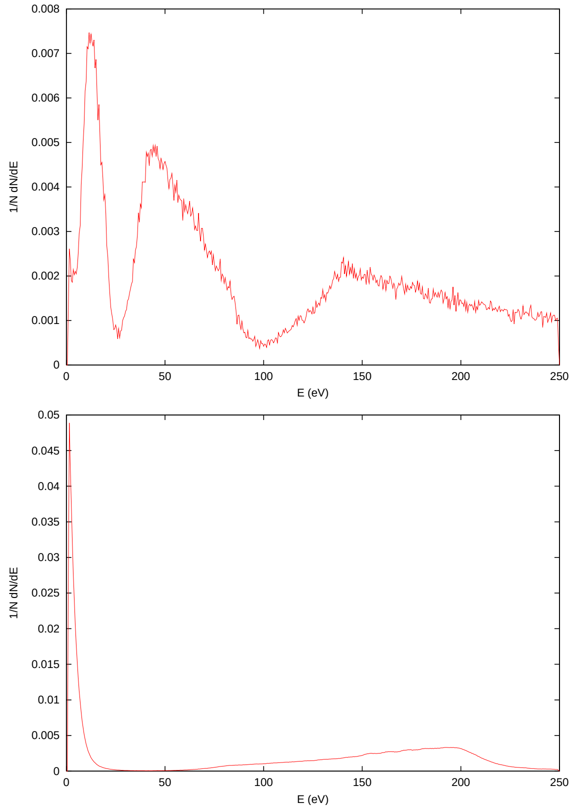

Figure 15: Energy distribution of electrons incident on LHC chamber wall for a chamber radius $r = 158$ mm (left) and 29 mm (right) [29].

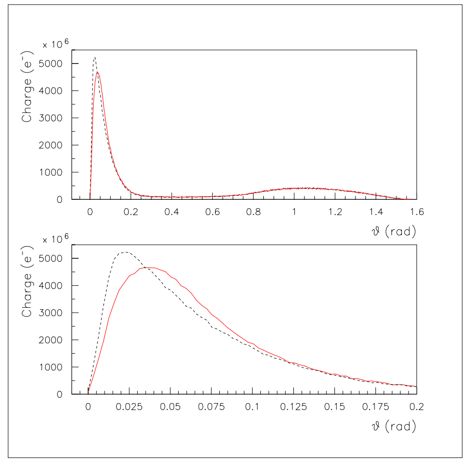

Figure 16: Angular distribution of electrons hitting the LHC beam pipe, simulated with (red) or without (black) including the beam magnetic field. [28].

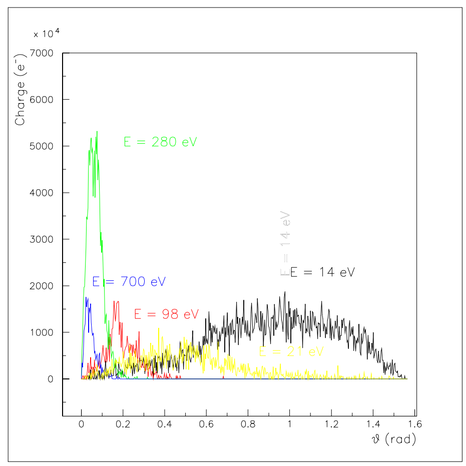

Figure 17: Angular distribution for different electron energies and LHC beam parameters [28]. Each curve refers to an energy interval of 7 eV.

Figure 17 demonstrates that the energy of the impinging electrons is strongly correlated with their angles of incidence.

The heat load deposited by the electron cloud on the beam screen inside the superconducting LHC magnets is of considerable concern, and during commissioning it may well constrain the operating parameters. Figure 18 compares the simulated average heat load per unit length in the LHC arcs, plotted as a function of bunch intensity, together with the cooling capacity available for the electron cloud. The various curves refer to different values of the maximum secondary emission yield. The cooling capacity was computed by subtracting from the total capacity the cooling needed for synchrotron radiation and impedance, which both increase with intensity. Figure 18 suggests that a maximum secondary emission yield not much larger than 1.1 is required in order to reach the design value of 1.1×10^{11} protons per bunch.

Electron cloud heat loads were also calculated for shorter bunch spacing as part of ongoing studies towards LHC luminosity upgrades [30]. Figures 19 and 20 show the simulated heat loads for various bunch spacings and intensities. In particular, they suggest a strong increase in the heat load if the bunch spacing is reduced from 25 ns to 10–15 ns. The heat load moderately improves for bunch spacings of less than 5 ns, where the gap is small compared with the bunch length.

In the limit of a constant current density and zero gap between the bunches, we reach the situation of a continuous beam. If the continuous beam is of finite length, *e.g.*, confined by rf barrier buckets, we may talk of a superbunch [31]. The electron-cloud heat load per proton in the beam for a superbunch is much smaller than for regular short bunches. In the ideal case of a coasting beam with constant line density, an electron emitted from the wall does not gain any energy in the static beam potential, but impinges on the opposing chamber wall exactly with its emission energy. The latter value is of the order of a few eV, for which the true secondary emission yield is negligible. Therefore, for a coasting beam the heat load due to the electron cloud is insignificant.

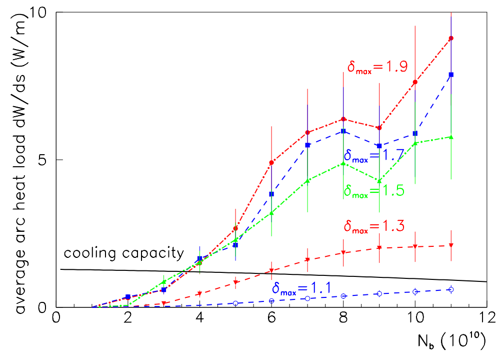

Figure 18: Average arc heat load and cooling capacity as a function of bunch population N_b, for various $\delta_{\max}$. Other parameters are $\epsilon_{\max} = 240$ eV, $R = 5\%$, $Y = 5\%$, and elastic electron reflection is included [5].

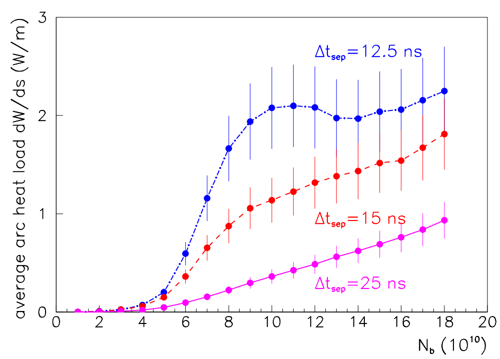

Figure 19: Average LHC arc heat load as a function of bunch population for bunch spacings of 12.5 ns, 15 ns, and 25 ns, and a maximum secondary emission yield $\delta_{\max} = 1.1$. Elastically reflected electrons are included.

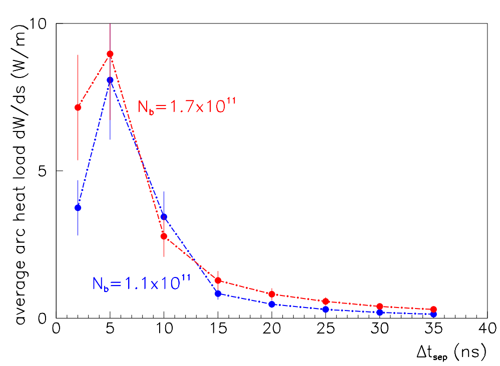

Figure 20: Average LHC arc heat load as a function of bunch spacing, for $\delta_{\max} = 1.1$ and various bunch populations.

If the beam does not occupy the entire circumference, but instead consists of one or more superbunches, electrons emitted near the end of the bunch may still acquire energy and initiate multipacting. However, if the superbunch is long with a constant current over most of its length, the fraction of multipacting electrons is small.

Figure 21 displays the simulated average electron energy deposition per passing proton and per meter length of beam line as a function of the full superbunch length, where we have considered a flat distribution with a linearly rising and falling edge of 10% each. For longer bunches the heat load per proton decreases clearly. This confirms the expected effectiveness of superbunches in suppressing the heat deposition from the electron cloud.

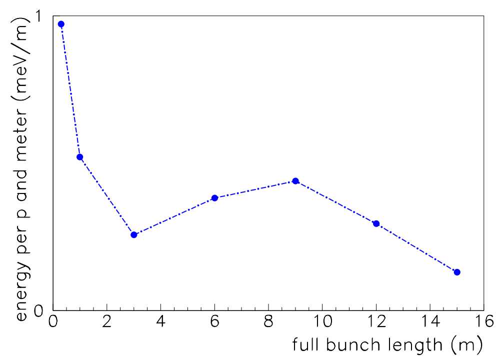

Figure 21: Average energy deposition per passing proton as a function of the full bunch length for an LHC dipole magnet, considering a constant flat top line density $\lambda = 10^{12}$ m^{-1} with 10% linearly rising and falling edge.

The LHC beam screen operates at a temperature of 5–20 K. It contains two rows of pumping slots, through which multipacting electrons could impinge on the cold bore of the magnet at 1.9 K, where little heat can be absorbed, and thus a magnet quench may easily be induced. The exact position of the multipacting electrons with respect to the foreseen location of the pumping holes is therefore an important design issue.

Already the earliest electron-cloud simulations have shown that in an LHC dipole magnet the electrons are not uniformly distributed, but concentrated in two vertical stripes [2]. This is illustrated in Figs. 22 and 23. The horizontal separation of the two stripes increases with increasing bunch population. For nominal intensities, corresponding to about 10^{11} protons per bunch and a chamber radius of about 2 cm, the horizontal distance between a stripe and the beam is 0.5–1 cm. For bunch populations of less than 5×10^{10} protons, the two stripes merge into a single stripe at the center of the chamber.

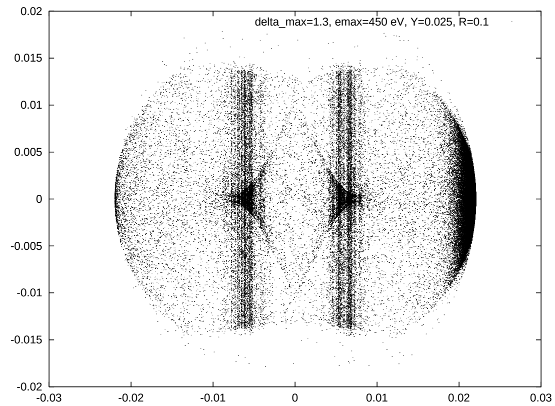

Figure 22: Snapshot of transverse e^- distribution in an LHC dipole chamber, simulated in 1997 [2]. Parameters were $\delta_{\max} = 1.3$, $\epsilon_{\max} = 450$ eV, $R = 0.1$, and $Y^* = 0.025$.

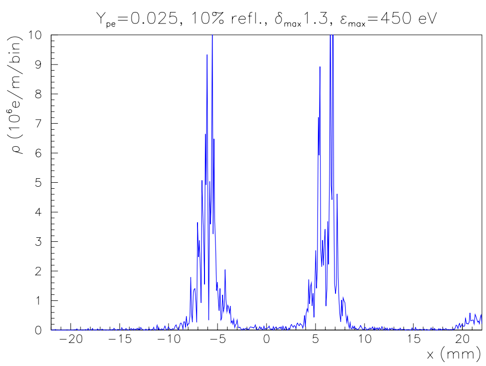

Figure 23: Projected horizontal electron charge density after 60 bunches in an SPS dipole chamber. Vertical peaks correspond to regions with large secondary emission. Parameters: $\delta_{\max} = 1.3$, $\epsilon_{\max} = 300$ eV, $R = 1$, pressure 50 nTorr, and 500 bins.

3 SINGLE-BUNCH EFFECTS

3.1 Ingredients

The simulation programme HEADTAIL for the single-bunch instability has been described in Refs. [32, 34]. The simulation models the turn-by-turn interaction of a single bunch with an electron cloud, which is assumed to be produced by the preceding bunches, and is newly generated on each turn, prior to the bunch arrival. Both the bunch and the electrons are represented by macroparticles. The electric forces acting between the two particle species are computed on a grid, using a Particle-in-Cell algorithm, that was originally written by D. Schulte for another purpose [33]. The momentum changes of electrons and beam macroparticles due to their mutual attraction are computed in time steps that correspond to the different longitudinal slices into which the bunch is subdivided. In the simulation, the interaction between beam and electrons occurs at one or more locations of the ring. In between the beam is propagated around the arcs of the storage ring, where the betatron motion in both planes is modelled by a rotation matrix. The synchrotron motion is included. Hence, the beam macroparticles slowly interchange their longitudinal positions, and in particular can move from one bunch slice to the next between turns. The effect of chromaticity is modelled by an additional rotation matrix which depends on the energy of each particle.

Finally, a regular transverse impedance, represented by a broadband resonator, as well as a proton space-charge force or beam-beam interaction can optionally be included, as discussed in Ref. [4], which also includes a table with typical simulation parameters.

3.2 Results

Figure 24 shows the transverse wake field induced by the electron cloud. In the simulation, the wake is computed by displacing a bunch slice transversely and calculating the resulting force on later portions of the bunch. The figure clearly demonstrates that the wake field depends on the longitudinal position. This is different from a regular wake field arising from the impedance of the vacuum chamber. For larger perturbations, the electron-cloud wake field also violates the superposition principle. Hence, the concepts developed for ordinary wake field and instabilities can only apply approximately, and care should be taken to watch the limits of applicability.

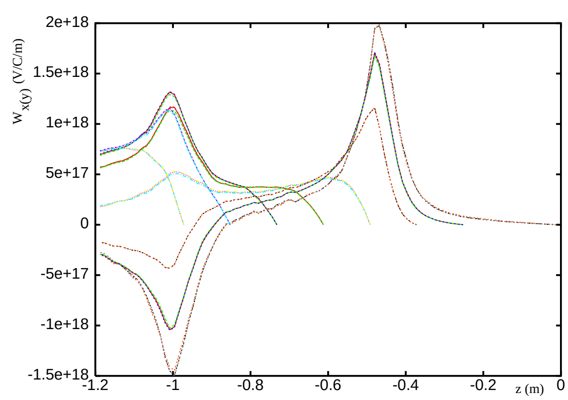

Figure 24: Simulated vertical wake field in V/m/C, excited by displacing various longitudinal slices inside the Gaussian bunch, vs. position in m, for an SPS field-free region. The bunch center is at -0.6 m, the bunch head ($2\sigma_z$) on the right.

In order to convert the wake field from the units V/C/m to m^{-2}, the numbers displayed must be multiplied by $4\pi/(Z_0 c) \approx 10^{-10}\ \Omega^{-1}\mathrm{sm}^{-1}$.

We have also evaluated the wake function for a bunch with uniform profile, *i.e.*, with a constant line density. The result is plotted in Fig. 25. The parameters are again those of the SPS, but the bunch population was adjusted so as to obtain the same electron oscillation frequency as found at the center of the Gaussian bunch in Fig. 24. The shape of the wake field does not much differ from that obtained for a Gaussian bunch, and the damped oscillation starts to approach the noise level after two full periods. In Fig. 25, the frequency of the wake oscillation is identical to the electron oscillation frequency, which for a uniform bunch of length L_b is uniquely defined as

$$\omega_{\mathrm{e}y(x)} = \sqrt{\frac{2N_b \mathrm{r_e c^2}}{\sigma_{y(x)} L_b (\sigma_x + \sigma_y)}} \ . \tag{18}$$

K. Ohmi has also computed the wake in a similar way for a uniform beam, *i.e.* and has then approximated the result by a broadband resonator, which is characterized by three parameters: quality factor Q_R, shunt impedance R_S/Q, and angular resonance frequency ω_R [35]. Given this type of parametrization, the TMCI threshold can be estimated using a formula derived by B. Zotter in 1982. For $\omega_R \sigma_z / c \gg 1$ the threshold bunch current is [36]:

$$N_{b,\mathrm{thr}} \approx \frac{6\pi^{3/2} Q_s Q_R \gamma (\omega_R \sigma_z / c)^2}{(c R_S / Q) \beta r_e}, \tag{19}$$

where β is the beta function, and Q_s the synchrotron tune.

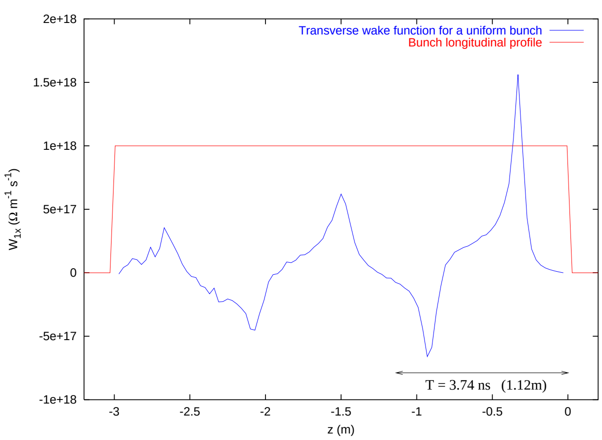

Figure 25: Simulated wake function excited by displacing the first slice of a 3m long uniform bunch for an SPS field-free region.

Figure 26 shows the simulated vertical bunch centroid motion and beam-size evolution over 12 ms for the CERN SPS, comparing a case with zero chromaticity and one with $\xi_y = 0.2$. The measured conventional SPS broadband impedance [37] was also included in this simulation.

In the SPS and LHC most of the circumference is occupied by dipole magnets. This has some consequences on the single bunch instability. Figure 27 compares the short range wake field simulated for a dipole field with that for a drift space, assuming the same initial electron distribution. In reality the initial distribution depends on

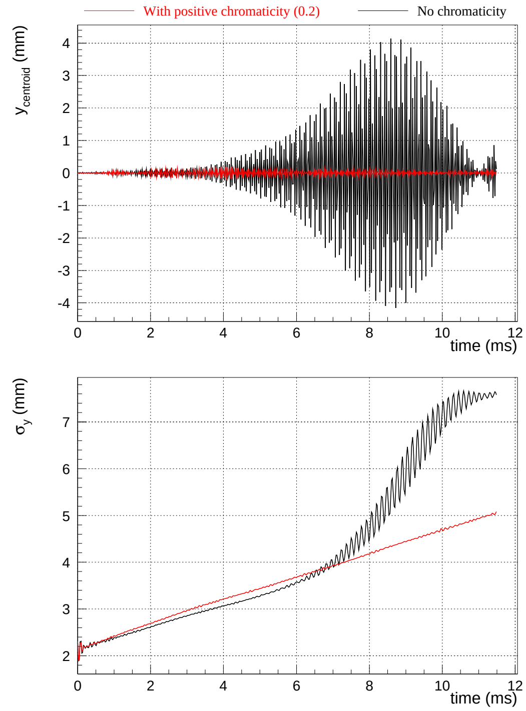

Figure 26: Simulated centroid motion and vertical beam size with zero and positive chromaticity ($\xi_y = 0.2$) in the SPS. A conventional wake field representing the machine broadband impedance is included in addition to the electron cloud [34].

the magnetic field, which will introduce further differences between field-free regions and dipoles. Regardless, the Fig. 27 shows that for the nearly round beam of the SPS the vertical wake field is weakened by the magnetic field. We attribute this to the absence of an electron pinch in the horizontal plane. The horizontal wake (not shown) is almost completely suppressed by the vertical magnetic field [38].

Figure 28 displays the simulated horizontal and vertical emittance growth in a dipole field and in a field-free region. As expected the dipole field suppresses the horizontal emittance growth and slows down the vertical.

It is also of interest to study the effect of a weak solenoid field on the interaction between a single bunch and the electron cloud, since presently solenoids have been wound over most of the circumference in KEKB and PEP-II to reduce the electron-cloud build up. The single-bunch simulation can show how such solenoid fields will affect the bunch evolution. Another motivation is the possibility of a 'controlled' experiment, which uses a detuned electron cooler to produce an 'electron cloud' of known density. Figure 29 shows the simulated electron phase space and the projection onto the x/σ_x axis, *i.e.*, the horizontal line density, a time $t = 1.2\sigma_z/\mathrm{c}$ after the passage of the bunch center, for three different solenoid fields, namely $B_z = 0$, 2.5, and 10 mT.

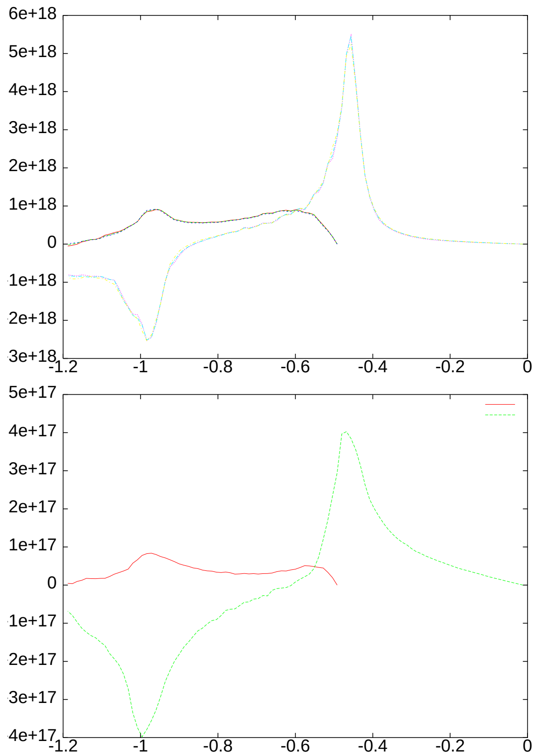

Figure 27: Simulated vertical wake field in V/m/C excited by displacing the 1st and 41st slice inside the Gaussian bunch, vs. position in m, for an SPS field-free region (left) and dipole field (right) and an electron density $\rho_e = 10^{12}$ m^{-3}. The bunch center is at -0.6 m, the bunch head ($2\sigma_z$) on the right [38].

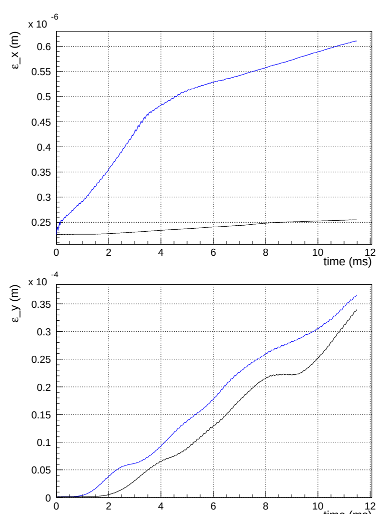

Figure 28: Simulated emittance growth in the SPS comparing a field-free region (blue) and a dipole field (black). Space charge is included, and an electron density of $\rho_e = 10^{12}$ m^{-3} is considered [38].

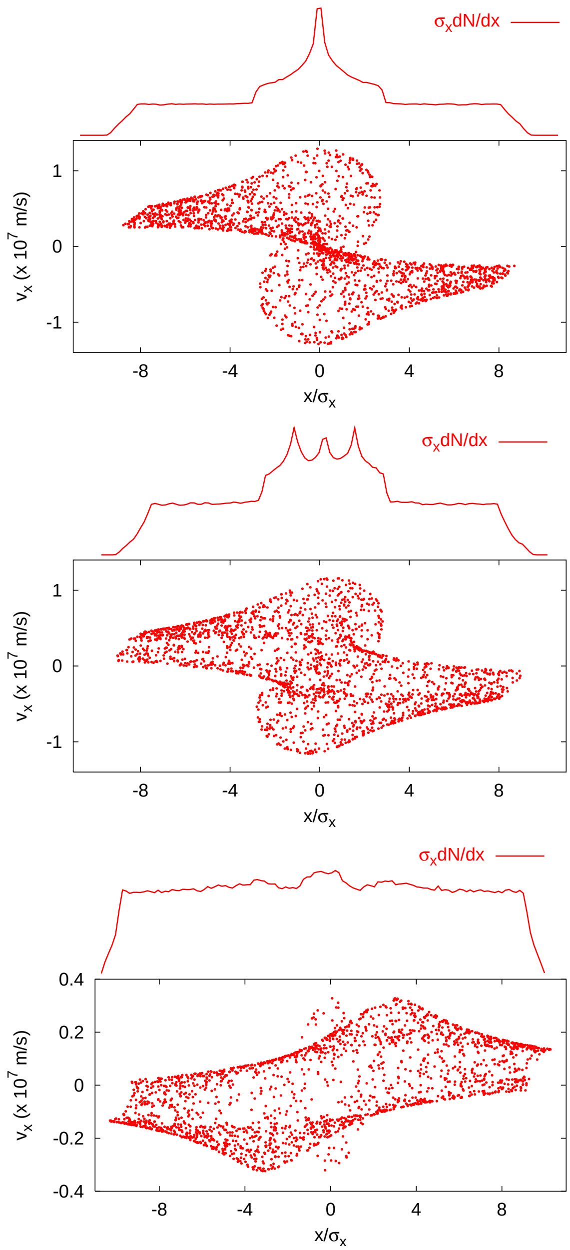

Figure 29: Electron phase spaces and horizontal line densities at $1.2\sigma_z$ behind the bunch center, for solenoid fields $B_z = 0, 2.5, 10$ mT.

The decrease of electron pinching with increasing solenoid strength is especially evident in Fig. 30, where all three horizontal projections have been superimposed on the same graph. The consequences still need to be studied by a full simulation of the bunch evolution, which is not limited to a single bunch passage.

However, we can already make a prediction by computing the short-range wake function in a solenoid field. The solenoid couples the horizontal and vertical motion of the electrons, and thus induces a normal wake and a skew wake. In order to characterize the wake field caused by the

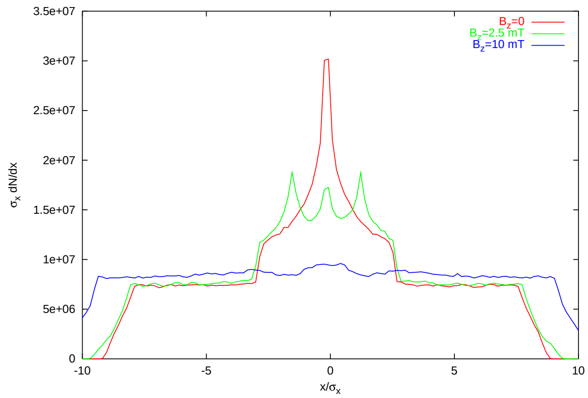

Figure 30: Electron densities along the x-axis at $1.2\sigma_z$ behind the bunch center, for solenoid fields of $B_z = 0$, 2.5, and 10 mT.

electron cloud in a solenoid, we displace a bunch slice in the horizontal direction only, and then compute both the vertical and the horizontal forces acting on the following parts of the bunch. Results for two solenoid field strengths are shown in Figs. 31 and 32. The wake function evaluated by horizontally displacing the first bunch slice is about one or two orders of magnitude lower than the one obtained in the case without a solenoid field. In this case both the horizontal and vertical trailing fields are normalized by the horizontal offset when computing the wake functions. The skew wake field, W_{1y}, is clearly nonzero and has a positive average value along the bunch, which is consistent with the expected effect of a solenoid coupling the horizontal and vertical motion of the electrons.

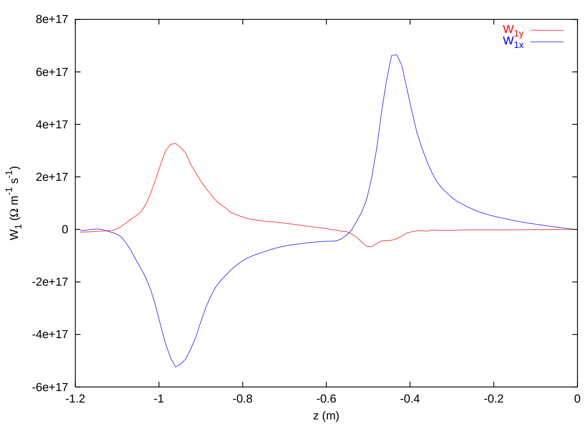

Figure 31: Transverse wake functions excited by horizontally displacing the first slice of a Gaussian bunch in a region with a 2.5 mT solenoid field.

4 CONCLUSIONS

We have discussed electron-cloud simulations modelling the build up of the electrons cloud, and simulations modelling the single-bunch instability that the electrons induces. Example results were presented for both types of studies.

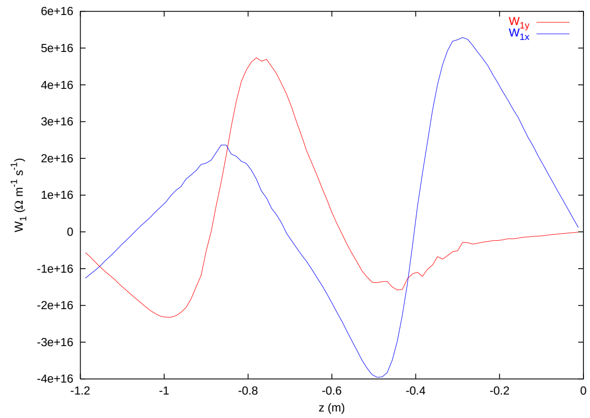

Figure 32: Transverse wake functions excited by horizontally displacing the first slice of a Gaussian bunch in a region with a 10 mT solenoid field.

The simulated accumulation of electrons due to beam-induced multipacting and photoemission is roughly consistent with observations. For several operating storage rings (SPS, PS, KEKB), the observed build-up time, electron density, and the number of electrons incident on the chamber wall are well reproduced in the simulation.

The simulation results for the single-bunch instability are also promising. The beneficial effect of a positive chromaticity found experimentally has been reproduced in the simulation [34]. Good agreement was achieved between K. Ohmi's PIC code and the program HEADTAIL written at CERN [39].

Space charge strongly modifies the effect of the electron cloud, as we discuss in a compagnion paper [4]. A similar synergy is expected for the beam-beam interaction.

A dipole field changes the single-bunch wake field and the instability. It completely suppresses the horizontal instability and also weakens the vertical. Also a solenoid field reduces the magnitude of the wake field, and, in addition, it gives rise to a skew wake, whereby, *e.g.*, a horizontal offset generates a vertical field.

We have presented preliminary evidence from our simulation that the electron cloud could become a major problem for future linear colliders.

In a dipole magnet and at sufficiently high bunch charge, two vertical stripes of enhanced electron density are formed inside the vacuum chamber by a beam-induced multipacting process. The measured horizontal positions of these stripes seem to agree with those predicted by simulations.

However, not every aspect of the measurements is well understood. For example, in the simulation we could not yet reproduce the SPS observation that the multipacting threshold is lower in a dipole magnet than in a field-free region. If this discrepancy is confirmed and cannot be explained by a weak residual stray field, it might indicate that the electron build-up simulation still misses some important physics.

5 ACKNOWLEDGEMENTS

We would like to thank a large number of colleagues for informations and helpful discussions, among others G. Arduini, V. Baglin, O. Brüning, I. Collins, K. Cornelis, H. Fukuma, M. Furman, O. Grobner, N. Hilleret, J.M. Jimenez, T. Katsouleas, K. Ohmi, K. Oide, M. Pivi, A. Rossi, F. Ruggiero, D. Schulte, and Y. Suetsugu.

6 REFERENCES

[1] G. Rumolo, F. Zimmermann, programme documentation at *http://wwwslap.cern.ch/collective/electron-cloud/electron-cloud.html*

[2] F. Zimmermann, "A simulation study of electron-cloud instability and beam-induced multipacting in the LHC", LHC Project-Report 95, and SLAC-PUB-7425 (1997).

[3] G. Rumolo and F. Zimmermann, "Longitudinal Wake Field due to Electron Cloud," these proceedings.

[4] G. Rumolo and F. Zimmermann, "Electron-Cloud Instability with Space Charge or Beam Beam," these proceedings.

[5] F. Zimmermann, "Electron-Cloud Simulations for SPS and LHC", Chamonix X, CERN-SL-2000-007 (2000); "Electron-Cloud Simulations: An Update", Chamonix XI, CERN-SL-2001-003-DI (2001).

[6] G. Rumolo et al., "Simulation of the Electron-Cloud Build Up and Its Consequences on Heat Load, Beam Stability and Diagnostics," PRST-AB 012801 (2001).

[7] I. Collins, private communication (2000).

[8] A. Chao, K. Oide, comments at this workshop (2001).

[9] S. Heifets, private communication (1997).

[10] J.S. Berg, "Energy Gain in an Electron Cloud during the Passage of a Bunch", LHC Project Note 97

[11] B. Richter, SLAC memo, unpublished (2000). (1997).

[12] R. Kirby and F. King, "Secondary Electron Emission Yields from PEP-II Accelerator Materials", SLAC-PUB-8212 (2000).

[13] V. Baglin, I. Collins, B. Henrist, N. Hilleret, G. Vorlaufer, "A Summary of the Main Experimental Results Concerning the Secondary Electron Emission of Copper," LHC-Project-Report-472 (2001).

[14] H. Seiler, "Secondary electron emission in the scanning electron microscope", J. Appl. Phys. 54 (11) (1983).

[15] M.A. Furman and G.R. Lambertson, "The Electron Cloud Effect in the arcs of the PEP-II Positron Ring," KEK Proceedings 97-17, p. 170, December 1997 (Proc. MBI97 workshop, KEK, Y.H. Chin, ed.) (1997).

[16] J.J. Scholtz, D. Dijkkamp, R.W.A. Schmitz, Philips J. Res. 50, 375–389 (1996).

[17] I. Collins, private communication (2001). CERN-SL-2001-003-DI.

[18] N. Hilleret, "An empirical fit to the true secondary electron energy distribution," unpubished draft, dated 23.10.01 (2001).

[19] W. Hoefle, "Observation of the Electron Cloud on Pick-Up Signals in the SPS," Proceedings Chamonix X.

[20] F. Zimmermann, CERN-SL-Note-2000-004 AP; CERN-SL-2000-017 (AP); CERN SL-Note-2001-022 AP; F. Zimmermann, H. Fukuma, K. Ohmi, CERN-SL-Note-2000-061 AP.

[21] F. Zimmermann, CERN-SL-2000-017 (AP)

[22] F. Zimmermann, H. Fukuma, K. Ohmi, CERN-SL-Note-2000-061 AP.

[23] M. Pivi, private communication of NLC parameters (2001).

[24] J. Jowett, T. Risselada, F. Zimmermann, H. Owen, "Damping Rings for CLIC," Proc. PAC'2001 Chicago, USA, CERN-SL-2001-038 (AP), and CLIC Note 494 (2001).

[25] K. Ohmi and F. Zimmermann, "Head-Tail Instability Caused by Electron Cloud in Positron Storage Rings", Phys. Rev. Letters 85, p. 3821 (2000).

[26] M. Furman and A. Zholents, "Incoherent Effects Driven by the Electron Cloud", PAC99, New York (1999).

[27] F. Zimmermann, "Electron-Cloud Simulations: An Update," Proc. Chamonix XI, CERN-SL-2001-003-DI (2001).

[28] A. Arauzo and F. Zimmermann, "Electron-Cloud Energy and Angular Distributions," CERN SL-Note-2000-057 AP (2000).

[29] A. Rossi, G. Rumolo, F. Zimmermann, "A Simulation Study of the Electron Cloud in the Experimental Regions of LHC," in preparation.

[30] F. Ruggiero, et al., report in preparation (2001).

[31] K. Takayama, J. Kichiro, M. Sakuda, M. Wake, "Superbunch Hadron Colliders," submitted to Physical Review Letters (2001).

[32] G. Rumolo, F. Zimmermann, "Theory and Simulation of the Electron-Cloud Instability," Proceedings of Chamonix XI, CERN-SL-2000-07 (DI).

[33] D. Schulte, Guinea-Pig programme for the simulation of beam-beam effects in linear colliders, unpublished.

[34] G. Rumolo, F. Zimmermann, "Simulation of Single Bunch Instabilities Driven by Electron Cloud in the SPS," Proc. PAC'2001 Chicago, USA, and CERN-SL-2001-041 (AP) (2001).

[35] K. Ohmi, F. Zimmermann and E. Perevedentsev, "Study of the Hast Head-Tail Instability caused by Electron Cloud," Proc. 18th International Conference on High Energy Accelerators (HEACC2001), Tsukuba, Japan, CERN-SL-2001-011 AP (2001).

[36] B. Zotter, "Transverse Mode Coupling and HEad-Tail Turbulence," CERN/ISR-TH/82-10 (1982).

[37] G. Arduini, H. Burkhardt, K. Cornelis, Y. Papaphilippou, F. Zimmermann, M-P. Zorzano, "Measurements of Coherent Tune Shifts and Head-Tail Growth Rates at the CERN SPS", EPAC 2000 Vienna, and CERN-SL-2000-027 AP (2000).

[38] L. Wang, G. Rumolo, K. Ohmi, F. Zimmermann, "Short Range Wake Field Caused by Electron Cloud in Bending Magnet," presented at APAC'01, CERN SL-2001-058 (2001).

[39] G. Rumolo, F. Zimmermann, H. Fukuma, K. Ohmi, "Electron Cloud Studies for KEKB," Proc. PAC'2001 Chicago, USA, and CERN-SL-2001-040 (AP) (2001).